

www.acsanm.org Article

Growth of Nanometer-Thick γ -InSe on Si(111) 7 \times 7 by Molecular Beam Epitaxy for Field-Effect Transistors and Optoelectronic Devices

Derrick S. H. Liu,* Maria Hilse,* Andrew R. Lupini, Joan M. Redwing, and Roman Engel-Herbert



Cite This: ACS Appl. Nano Mater. 2023, 6, 15029-15037

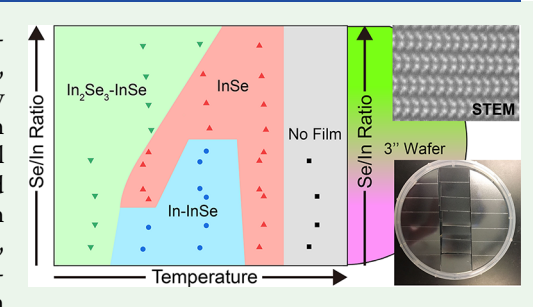


ACCESS

III Metrics & More

Article Recommendations

ABSTRACT: γ-InSe is a semiconductor that holds promising potential in high-performance field-effect transistors and optoelectronic devices. Large-scale, single-phase γ-InSe deposition has proven challenging because of the difficulty in precise control of stoichiometry and the coexistence of different indium selenide phases. In this study, we demonstrate the wafer-scale combinatorial approach to map out the growth window as functions of the Se/In ratio and growth temperature for γ-InSe on the Si(111) 7×7 substrate in molecular beam epitaxy. X-ray diffraction (XRD) was used to identify the indium selenide phases, while atomic force microscopy revealed four distinct surface morphologies of γ-InSe, enabling a discussion of the growth mechanisms associated with each



morphology. Cross-sectional atomic resolution scanning transmission electron microscopy confirmed that the film was of high crystalline quality and had nearly single-phase γ -InSe. Our comprehensive study elucidates the In—Se phase map for thin film growth parameters, providing invaluable landmarks for the reproducible synthesis of high-quality γ -InSe layers.

KEYWORDS: InSe, molecular beam epitaxy, chalcogenides, two-dimensional materials, large-scale synthesis

INTRODUCTION

Two-dimensional (2D) chalcogenide-based thin films have had growing interest in the scientific community in the past decade. These layered materials are composed of stacks of single layers in the form of monochalcogenides MX, dichalcogenides MX_2 , and sesqui-chalcogenides M_2X_3 (M = In, Ga, Sn, Pt, Mo, W, Bi, Sb, Nb; X = S, Se, Te). Their unique electronic states result in promising novel functionalities such as high mobility semiconductors, 1-345 ferroelectrics, 6-89 topological insulators, 10-121314 and superconductors, 15-1718 just to name a few. InSe gained renewed interest among the monochalcogenide material family owing to its wide range of applications. The quantum confinement-induced direct-to-indirect bandgap transition, from 1.26 eV in bulk to up to 2.6 eV in a single layer, makes InSe an intriguing candidate for optoelectronic and photo response applications. ^{2,19,20} In addition, InSe has been reported to possess an electron mobility of up to 1000 cm²/V·s at room temperature because of its small effective electron mass of $0.143m_0$. Furthermore, the relatively low growth temperatures that are required to ensure sufficient surface diffusion for enhanced crystallinity favor the integration into existing back-end-of-line (BEOL) semiconductor processing. The scalability down to a single layer accompanied by the BEOL-friendly synthesis parameters makes InSe a promising candidate as a channel material in high-performance, ultrathin body field-effect transistors (FET). To date, exfoliation from a single crystal is the most commonly used approach to study

the electronic properties of InSe, 1,2,4,19,22-24 while large-scale synthesis with precisely controlled thickness is still required for realistic industry purposes. Thin film synthesis techniques like pulsed laser deposition, 3,25 physical vapor deposition, 26,27 metal—organic chemical vapor deposition, 5,28 and molecular beam epitaxy (MBE) have successfully been demonstrated for InSe thin film growth. ^{29–3132} MBE has advantages over other methods in growing high-quality crystalline InSe films, as it excels in precise control of atomic flux, growth temperature, and deposition rate. Despite the strength of precise control of growth parameters, growing a phase pure InSe film generally requires an extensive growth window mapping process. This is due to the many In-Se phases that coexist in nature and Se's much higher volatility than In. 33,34 Regardless of the targeted In-Se phase, Se must always be oversupplied to mitigate the loss in re-evaporation from the growth front. In addition, reported growth parameters are generally only a guide for approaching the stabilization of a specific In-Se phase due to the differences in reactor design, geometry, and methodology

Received: June 9, 2023 Accepted: July 24, 2023 Published: August 4, 2023





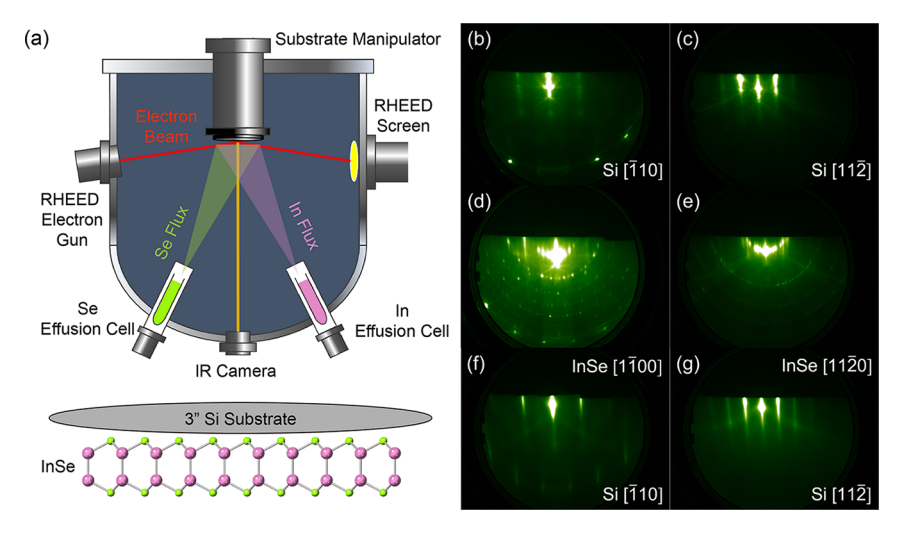


Figure 1. (a) Schematic of MBE reactor for InSe growth and InSe on 3 in. Si(111) wafer. (b and c) Before annealing RHEED diffraction pattern with the azimuthal incident electron beam along the $[\overline{1}10]$ and $[11\overline{2}]$ directions of Si(111). (d and e) RHEED diffraction pattern taken in the same two azimuths after annealing to 800 °C for 1 h. (f and g) RHEED diffraction pattern taken in the same two azimuths after InSe growth.

used between systems, which is a challenge for reproducibility in the field. With this work, we demonstrated a strategic approach to systematically map out the growth window of InSe on Si(111) substrates in MBE. 35,36 The composition and phase identification of the films were determined by X-ray diffraction (XRD). A spiral growth mode, which is commonly seen in the synthesis of other 2D chalcogenide-based materials, and a layer-by-layer growth mode for InSe were both observed by atomic force microscopy (AFM). The mechanism behind the observed spiral growth mode of quadruple-layered InSe that relates similarly to tri- and quintuple-layered materials, such as WSe₂, MoS₂, Bi₂Se₃, and In₂Se₃, is discussed and related to the growth environment. 37-39 Scanning transmission electron microscopy (STEM) is used to visualize the atomic arrangements within the film in the cross section and verified the polytype of InSe on Si(111) as γ -InSe with a small polytype impurity. The results demonstrate that the In atoms bond first to the Si top surface, followed by the subsequent formation of a half-quadruple layer of InSe at the interface.

■ EXPERIMENTAL SECTION

InSe films were grown on 3 in. epi-ready, p-type boron-doped Si(111) wafers (CrysTec). Each wafer was first degreased with 5 min ultrasonication in acetone, methanol, and DI water at room temperature in sequence. Following the degreasing step, the wafers were cleaned in 80 °C RCA-1 solution for 10 min to remove residual organics and form a thin silicon oxide layer. The oxide layer was subsequently etched away with 10:1 buffered hydrofluoric acid. After removal from the etch, the wafer was soaked in 40% NH₄F solution for 2 min at room temperature to generate the atomically smoothed Si(111) 1 × 1 H-terminated surface. To prevent reoxidation, the wafers were immediately loaded into the load lock chamber, which was later pumped down to around 5 × 10⁻⁷ Torr before outgassing substrates at 200 °C for 60 min in the load lock to remove residual water films.

The Si(111) 1 \times 1 to 7 \times 7 surface reconstruction was achieved by a thermal treatment for 60 min at 800 °C with a ramp rate of 20 °C/min in ultrahigh vacuum (UHV) upon loading substrates into the growth chamber. In situ reflective high energy electron diffraction (RHEED) was used to monitor and confirm the surface reconstruction process, as well as the InSe thin film growth. Immediately after the UHV anneal, the Si(111) substrate was cooled down to growth temperature with a ramp rate of 50 °C/min. InSe growth was carried out in an R450 MBE reactor (DCA Instruments).

During the growth, the background pressure was around 5×10^{-10} Torr. In and Se atomic fluxes were calibrated with a quartz crystal microbalance (QCM) at the film growth position. In fluxes were generated by using a dual-temperature Knudsen effusion cell at 840 $^{\circ}$ C, which resulted in an In flux of around 2.8 \times 10¹³ atoms/cm⁻² s⁻¹ and a growth rate of 0.15 Å/s. Se was supplied from a lowtemperature Knudsen effusion cell operated between 125 to 135 °C, depending on the target Se to In flux ratio. The Se and In tooling factors for QCM flux calibration were previously determined from physical thickness measurements on calibration samples using X-ray reflectivity and scanning electron microscopy (SEM). An Optris Xi80 infrared (IR) camera was installed to serve as an additional substrate temperature metric along with the system's thermocouple installed behind the substrate. Figure 1a schematically shows the components of the MBE reactor and the crystal structure of InSe. The film target thickness was set to 30 nm in all growth campaigns of the presented work.

Phase examination of the samples was determined by acquiring high-resolution 2θ - ω -scans using Cu-K_{α 1} XRD from a Malvern PANalytical 4-Circle X'Pert3 materials research diffractometer. The film thickness was extracted by Scherrer equation calculation with a shape factor of 0.89, a wavelength of 1.5406 Å, and a 0.012° full width at half-maximum (FWHM) from the instrument. FWHM of the InSe peaks were obtained by applying a pseudo-Voigt fitting profile to the out-of-plane 2θ – ω -scans XRD data. The surface morphology of the InSe films was captured by a Bruker Dimension Icon atomic force microscope (AFM) operating in peak force tapping mode. STEM was performed in a Nion UltraSTEM 200 operating at 200 kV. The images were acquired in the high-angle annular dark-field (HAADF) imaging mode in which the contrast varies with approximately the square of the atomic number and the projected thickness. Samples were prepared in a cross-section view, by thinning to approximately 10 μ m, then ion-milling, and images of several films were acquired, viewing down the $[\overline{1}10]$ and $[11\overline{2}]$ axes. The characterization data and synthesis parameters of the samples presented in this work can be accessed through ScholarSphere.55

■ RESULTS AND DISCUSSION

The lower surface energy Si(111) 7×7 surface was achieved by UHV annealing in the growth chamber prior to deposition. Due to system constraints, a thermal anneal of 800 °C for an hour was applied to stabilize the Si reconstruction instead of flashing the substrate to above 1100 °C as others report. Figure 1b–g shows the RHEED patterns taken along the [110] and [112] incident beam azimuth of Si(111) at different

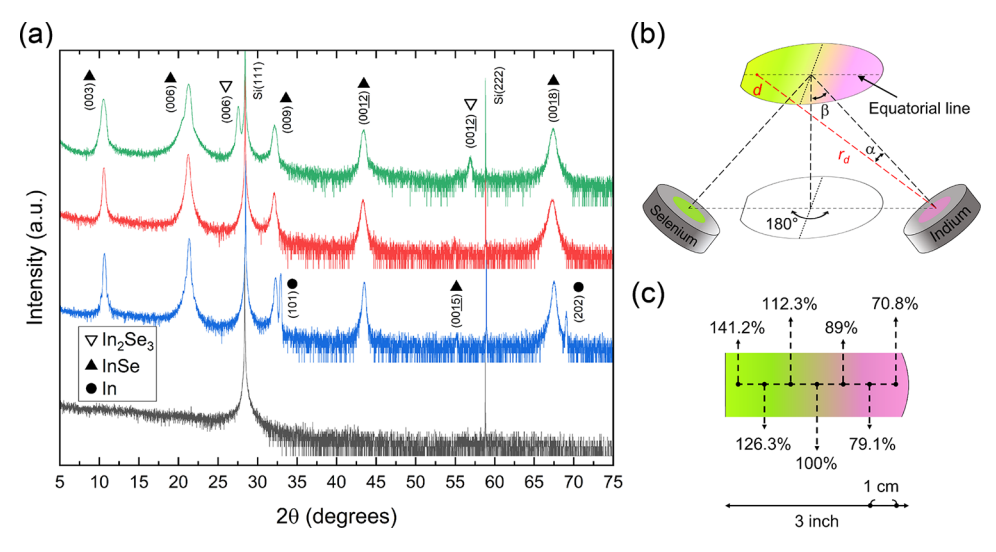


Figure 2. (a) XRD $2\theta-\omega$ -scans of In–Se phases found in the InSe growth window mapping process. Top: In₂Se₃–InSe mixture in green. Second from top: single-phase InSe in red. Second from bottom: In–InSe mixture in blue. Bottom: No film growth. (b) Schematic setup of flux ratio mapping approach in MBE across a 3 in. wafer substrate. (c) Flux ratio (Se/In) distribution across the equatorial line of a 3 in. Si(111) wafer calculated for the setup in (b).

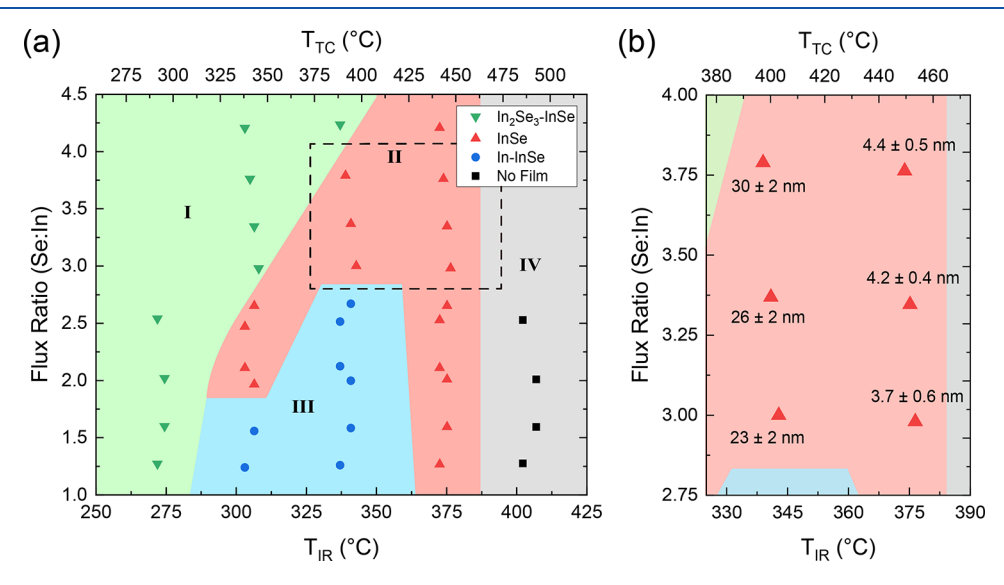


Figure 3. (a) Indium selenium growth map as a function of the growth temperature and flux ratio. Both the IR camera temperature $T_{\rm IR}$ and thermocouple temperature $T_{\rm TC}$ are given for completeness. (b) Film thicknesses in the dotted line rectangle of (a).

growth stages. The clear Kikuchi lines and lattice streaks in the RHEED before UHV annealing, i.e., Figure 1b,c and after, Figure 1d,e indicate that the substrate surface was very smooth after the chemical etch process. The formation of additional diffraction intensity distributions along Laue circles in Figure 1d,e after UHV anneal was in excellent agreement with the well-documented 7 × 7 dimer-adatom rearrangement of the top Si bilayer atoms. 41,45,46 The lower surface energy of the Si(111) 7 × 7 reconstructed surface is expected to favor van der Waals epitaxy compared to the energetically higher nonreconstructed Si(111) surface. 47-49 InSe RHEED patterns taken after the growth in Figure 1f,g show lucid streaks and a dark background, suggesting a high-quality single-crystal film was epitaxially grown on the Si(111) substrate. The epitaxial orientation relationship between Si and InSe was deduced from the RHEED in Figure 1 to Si[111] | InSe[0001] with $Si[1\overline{10}]$ || InSe[1\overline{1100}].

Mapping the In-Se thin film growth parameter space of flux ratio (Se/In) and growth temperature systematically, a variety of phases were found in the 4.25 to 1.25 Se/In flux ratio window and a growth temperature window of 275 to 375 °C, evaluated by $2\theta-\omega$ out-of-plane XRD scans shown in Figure 2a. Obtained films were sorted into four categories (green, red, blue, and black) and arranged with Se-rich at the top and Inrich at the bottom in Figure 2a. Under the Se-rich condition green category, an In₂Se₃ peak was observed along with the peaks of the (00m) plane family of InSe with $m = 3 \times p(p \in \mathbb{N})$, indicating a mixed-phased film. The film was single-phase InSe as the oversupply of Se was slightly reduced in the red category. Under the In-rich conditionblue category, excessive indium crystals were present in the film as peaks originating from the (n0n) plane family of pure In were measured. Finally, at elevated temperatures, presented in category IV in black in Figure 2a, the sticking coefficients of Se and In on the Si(111) substrate were near zero so that no film

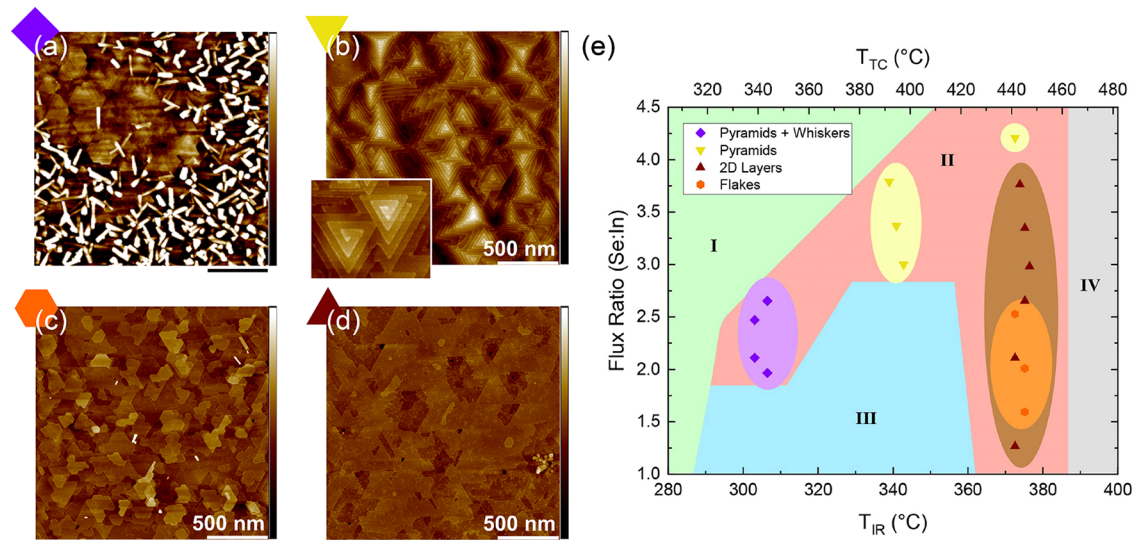


Figure 4. (a) InSe film with regions of flat and needle-like surface morphology. The scale bar under the figure represents 500 nm. (b) InSe film with a triangular spiral pyramid surface morphology. The inset shows a pyramid with a clockwise spiral and the other pyramid with a counterclockwise spiral. (c) InSe film composed of flakes in triangular or hexagonal shapes. (d) InSe film with a smooth surface morphology of coalesced few-layered coverage. The height scale bars on the right of the images represent 10 to 0 nm. (e) Single-phased InSe surface morphology map as a function of growth temperature and flux ratio.

was detected after growth. As the growth window for both flux ratio and the temperature was found to be very narrow to obtain single-crystal, single-phase InSe growth, a combinatorial growth approach as sketched in Figure 2b,c was applied.³⁵ This growth approach utilizes the elemental sources' geometrical arrangement and the sizable substrate surface area of full 3 in. wafers to substantially speed up the growth window mapping process while enhancing the precision in flux ratio control by MBE.³⁶ The schematic relative position of effusion cells and substrate for the MBE system used for this study is shown in Figure 2b. During the growth, the substrate manipulator stayed stationary while the flat side of the wafer was aligned to the Se cell. As a result, a flux ratio gradient parallel to the equatorial line of the wafer was generated, as shown in Figure 2c. The flux ratio profile across the wafer can be calculated by using the calibrated indium and selenium fluxes. For example, the In atomic flux density at position d can be described with the equation: 50

$$\Phi_d^{\rm In} = \Phi_{\rm center}^{\rm In} \frac{r}{r_d} \frac{\cos \alpha}{\cos 0} \frac{\cos(\alpha + \beta)}{\beta}$$

temperatures but varying Se/In flux ratios.

where $\Phi_{\mathrm{center}}^{\mathrm{In}}$ is the In atomic flux at the center of the sample manipulator and r_d is the travel distance from the center of the Knudsen cell opening to position d on the wafer. α is the angle between the working distances to the center of the wafer and position d, and β is the effusion angle with respect to the substrate normal. Therefore, the local flux ratio at position d on the wafer can be determined as $\frac{\Phi_d^{\mathrm{ls}}}{\Phi_d^{\mathrm{ln}}}$. Following this calculation for the MBE system used over a full 3 in. wafer, the flux ratio variation across the entire wafer is about 70%. The flux ratio differences at each position compared to the center are shown in Figure 2c. For a single-growth campaign on a 3 in. wafer, a total of seven $10 \times 10 \text{ mm}^2$ samples were split from the full 3 in. wafer according to the distances given in Figure 2c and characterized individually, each reflecting identical growth

An In-Se thin film phase map as a function of flux ratio and growth temperature was composed of the combinatorial growth XRD analysis, as shown in Figure 3a using the previously introduced categories. Predictably, the In₂Se₃-InSe mixed-phase films (green) were found either in growth at low temperatures or under high flux ratios. This mixed-phase region was labeled I in Figure 3a and started with films grown at 271.9 °C with a flux ratio of 1.274 and ended with films grown at 337.1 °C with a flux ratio of 4.236. In this region I, the In₂Se₃ phase resulted most likely from the oversupply of Se, which was associated with too high of a flux ratio or less Se reevaporation from the film caused by insufficient temperature. Any film grown with either even lower or higher flux ratios or lower temperatures than the green category displayed in Figure 3a is expected to be mixed-phase In₂Se₃-InSe or even singlephased In₂Se₃. Single-phased InSe—red category II—could be obtained when the oversupply of Se was reduced by either increasing the growth temperature or reducing the supplied Se flux ratio. For example, increasing the growth temperature for a film at 308 °C with a flux ratio of 2.98—green mixed-phase slightly to about 320 °C would move this film into the red single-phased region II as less Se was effectively incorporated into the film under the slightly altered growth conditions. However, reducing the flux ratio beyond a certain value (1.75 for temperatures around 300 °C and 2.75 for temperatures around 325 to 350 °C) could also result in a transition into the blue region III of excessive In left on the film surface. This Serich to In-rich growth transition was clearly seen when moving down the columns of samples grown at around 300 and 337.5 °C. Furthermore, each region's relative position moved upward (toward higher flux ratios) as the temperature increased from around 300 to 337.5 °C. This could be explained by an overall decrease in the sticking coefficient of Se as the growth temperature increased. As the growth temperature reached around 375 °C, all films were found to be single-phased InSe, suggesting elemental In also has a nonunity sticking coefficient on Si(111) at this temperature. The reduction of the film thickness supports this assumption as well. Figure 3b shows the

film thicknesses of the samples highlighted with a dotted rectangle in Figure 3a. The consistent film thickness reduction for samples that were grown at a close flux ratio but with higher temperature supports the assumption of In sticking coefficient decrease. Additionally, the higher flux ratio generally led to thicker films as more Se could incorporate into the film. The direct transition of mixed-phase In₂Se₃—InSe—category I—to In-rich InSe—category III—can be related to a sharp drop of the Se sticking coefficient, which was reported earlier for pure Se deposition at much lower temperatures. S1,52 At even higher temperatures around 400 °C, no film growth was observed on the Si surface, suggesting that both Se and In had a nearly zero sticking coefficient at these growth temperatures.

Surface morphologies of single-phase InSe films investigated with AFM are shown in Figure 4. The different morphologies observed across all our samples were generalized and categorized into four types as seen in Figure 4a-purple diamond for films with smooth regions and regions with needle-like surface features, Figure 4b—yellow triangle for films with triangular spiral pyramid surface morphology, Figure 4c—orange hexagon for films composed of individual patches of flakes, and Figure 4d—brown triangle for films that exhibit smooth surfaces of coalesced few-layered coverage. The overlay of the surface morphology types and their respective growth parameters are shown in Figure 4e building upon the In-Se thin film phase diagram from Figure 3a. As presented in Figure 4a, the films that were grown with flux ratios ranging from around 1.9 to 2.7 and temperatures between 300 and 310 °C were covered by randomly oriented needle-like features. Under the needles was the signature triangular spiral topology of chalcogenide-based 2D materials such as Bi₂Se₃ and WSe₂. We thus deduced that the needle features were most likely randomly oriented In₂Se₃ crystals as they were also seen in all of the mixed-phase In₂Se₃—InSe film samples. After the growth temperature was increased to about 340 °C and the flux ratio increased from 3 to 3.8, needle formation was suppressed, and the triangular pyramid structure of InSe was revealed, as shown exemplarily in Figure 4b. At a temperature of 375 °C, there were two types of topographies for the InSe film present. Most of the films exhibited smooth few-layered coalesced growth with a triangular layer outline, as illustrated in Figure 4d, which is expected for a van der Waals material, such as InSe. However, there were some cases in which the morphology consisted of a mixture of triangular and hexagonal flakes, as depicted in Figure 4c. The overall topography was still following the two-dimensional stacking characteristic, and the random shape of the crystal could relate to the thermal equilibrium of the growth condition. It is worth pointing out that the morphology of the largest flux ratio sample at 375 °C showed triangular spiral pyramid growth, indicating that excessive supply of the chalcogen element to the growth front could trigger the spiral growth mode. The surface morphology map of single-phase InSe in different growth parameters is shown in Figure 4e.

Theories explained the mechanism of out-of-plane spiral triangular pyramidal growth that appears to break the layer-by-layer crystal structure and morphology with nonequal growth speed of two different material edges: the fast growth rate, i.e., zigzag, and the slow growth rate, i.e., armchair edge. ^{37,39} The growth rate difference along with the initial InSe nucleus placement with respect to other islands or substrate step edges could trigger what further appears as a screw dislocation

center. Figure 5a shows the top view of a schematic single quadruple layer InSe nucleus. The red line represents the

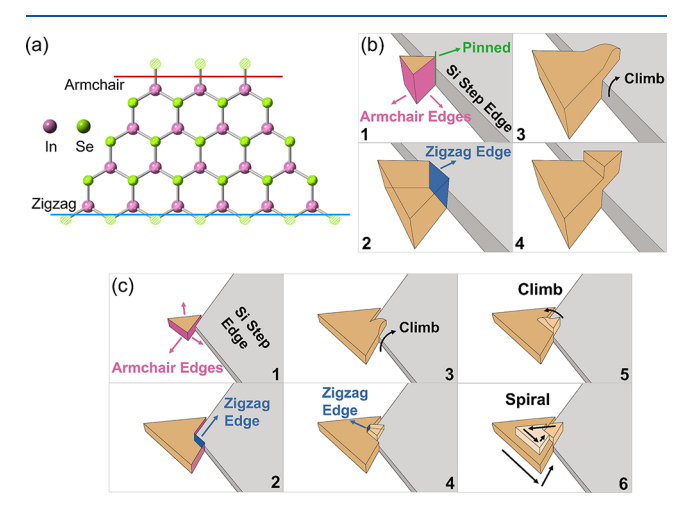


Figure 5. (a) Top view of a single InSe layer flake sketching its atomic arrangement. The pink line intercepts the In armchair edge, and the blue line intercepts the In zigzag edge. (b) Schematic lateral expansion flow of an InSe nucleus climb over a Si(111) step edge. (c) Schematic lateral expansion of an InSe nucleus and spiral growth mode triggered by a step-edge corner.

slower growth rate In-terminated armchair edge, and the blue line illustrates the faster growth rate In-terminated zigzag edge. As a free-standing InSe nucleus expands, the fast growth rate, i.e., zigzag edge, will grow itself out of existence, resulting in a triangular island composed of slow armchair edges. Two scenarios of the nucleus and substrate step-edge interaction are illustrated in Figure 5b,c, respectively. In Figure 5b, one of the fast-growing facets was pinned by a Si(111) step edge. Therefore, the fast-growing zigzag edge extended parallel to the Si(111) step edge as the InSe free-standing nucleus continued to expand on the free edges, and a trapezoid-shaped island emerged. However, the van der Waals nature of InSe provided room for part of the crystal to "climb" over the step edge and stretch vertically with a Si(111) step height of about 0.31 nm. 53,54 After the free-standing island climbed over the step edge, it gradually reshaped back into a triangle due to the fast-growing zigzag edge growing itself out of existence once again. Another scenario in which the InSe nucleus was intercepted by a corner of the Si(111) step edge is shown in Figure 5c. In this case, the InSe nucleus was not able to climb directly over the step edge as the pinned growth front was a slow growth rate armchair edge. Instead, the InSe island developed into a triangle that is cut off by the Si(111) stepedge corner. A fast-growing zigzag edge with a growth direction parallel to the cropped triangle corner emerged during crystal expansion. This fast-growing front climbed over the step edge to recover the triangular shape of the InSe crystal, similar to that in Figure 5b. Nevertheless, the InSe crystal that is located on the Si(111) step edge also acted as a free-standing nucleus. The new nucleus (brown) was pinned by the first nucleus (dark brown) when attempting to grow into a triangle crystal with solely armchair edges. An identical climb-expansion process occurred subsequently as the second nucleus (brown) generated a third free-standing nucleus (light brown). The second nucleus pinned later the third nucleus as more material was supplied to the growth surface. This repeating process not only resulted from the interaction

between free-standing InSe nuclei and Si(111) step edges but was also caused by InSe nuclei with height differences merging into a coalescing layer. As the Si(111) substrate was fully covered by the InSe film, numerous spiral centers on the growth surface led to the topography shown in Figure 4b, in which the spiral pyramids with an arithmetic progression in vertical sizes portrayed the film surface morphology.

Nie et al. pointed out that the spiral centers of the chalcogenide-based 2D materials could arise from metal vacancy formation between two different growth edges.³⁸ Metal vacancies in the chalcogen-rich condition distorted the local planar structure as the armchair edge and zigzag edge from adjacent islands expanded toward each other. The local distortion prompted the island with the zigzag edge as the connection front to climb over the adjacent island instead of merging into a coalesced film, resulting in the spiral growth mode described above. Both explanations of fast growth facet interaction with substrate step edge as well as metal vacancy support our finding that the InSe triangular pyramids were found under Se-rich conditions. On the other hand, the fastgrowing zigzag facets and In vacancies were likely suppressed in the In-rich growth conditions, giving rise to the smooth layered or flake-like film morphology.

High-resolution cross-sectional high-angle annular dark-field STEM imaging was performed along the Si(111) [110] zone axis on the single-phase InSe film to examine the microstructure, as shown in Figure 6a. The substantial atomic

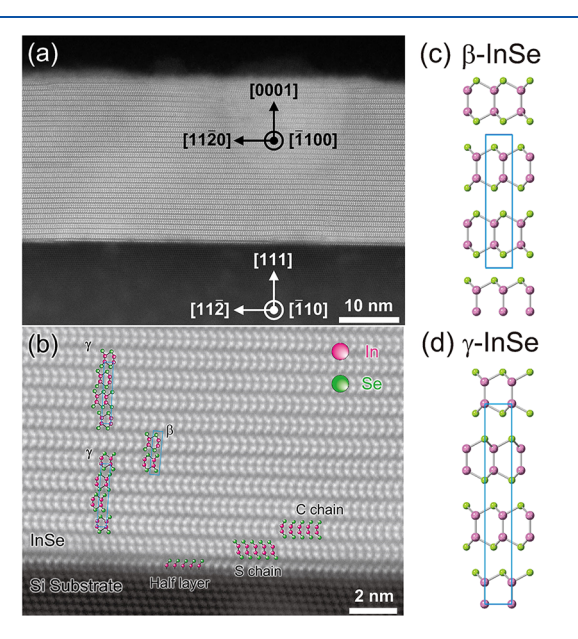


Figure 6. (a) HAADF STEM image of InSe on Si(111). (b) HAADF STEM image of InSe on Si(111) at high magnification. The In and Se colored notations are included to help visualize the In–Se–Se–In chain shapes and stacking sequences. (c) Sketch of the β-InSe crystal structure along the b axis. (d) Sketch of the γ-InSe crystal structure along the b axis.

number difference between In, Se (bright), and Si (dark) gives rise to a clear contrast between the film and the substrate. About 30 InSe quadruple layers were captured, generally agreeing with the nominally expected film thickness of about 25 nm. The high-resolution image in Figure 6b visualizes the epitaxial growth of γ -InSe on Si(111) with the crystallographic orientation of γ -InSe[1120]|| Si[1112], γ -InSe[1100]|| Si[110], and γ -InSe[0001]||Si[111]. Surprisingly, the initial layer of γ -

InSe started with half of a quadruple layer on Si(111), giving the interface structure In-Se rather than In-Se-Se-In. This implies that single-layer InSe on Si(111) prepared with a 7×7 reconstruction is not possible. Single-layer InSe growth thus requires differently terminated Si(111) surfaces or other growth platforms. In addition, the first quadruple layer that followed the half layer on the interface did not exhibit the expected C shape for 2D InSe, in which the Se-In-In-Se chains possess horizontal mirror symmetry. Alternatively, the first quadruple layer showed S-shaped Se-In-In-Se chains, in which the Se atoms were located at opposite sides of the vertical In-In bonds. Regardless of the local disorder near the interface, the STEM images confirm that there was no surface reoxidization of the Si(111) substrate after the chemical substrate preparation etching procedure, but showed high interface quality.

The polytypes of InSe were distinguished by the stacking sequences of the quadruple layer. Figure 6c,d shows the crystal structure of β -InSe and γ -InSe. In the higher magnification STEM image, as shown in Figure 6b, the film was found to predominantly consist of γ -InSe with the presence of minor β -InSe regions. From the first C shape quadruple layer, the third layer formed repeating γ -InSe unit cells. However, a 180° rotation occurred between the fourth and fifth layers, resulting in a twin domain boundary and a β -InSe unit cell insert. The stacking sequence of the quadruple layers above the fifth layer remained in the γ -InSe ABCABC stacking, with one-third of unit cell translation between each layer.

CONCLUSIONS

In summary, we display the large-scale synthesis of the γ -InSe film on a 3 in. Si(111) substrate by MBE for high-performance FETs and optoelectronic devices. The growth window of γ -InSe as a function of flux ratio and growth temperature was systematically mapped out through a combinatorial growth approach. Single-phased γ -InSe could be obtained in a wide range of flux ratios at temperatures around 375 °C, at flux ratios between 3 and 3.75 at 337.5 °C, and at flux ratios from 2 to 2.75 at 300 °C. A substantial film thickness reduction with respect to the target thickness occurred at 375 °C. In contrast, the actual thickness-to-target thickness ratio remained close to unity at 337.5 and 300 °C. We further untangle the interconnected relationship between the two growth parameters and the film phases, as well as the film surface morphology. Four surface morphologies were found in our single-phased films. The mechanism behind the spiral growth mode and layered growth mode is strongly associated with the initial nucleus expansion in Se-rich or In-rich environments. STEM images have revealed that the film was mainly single-crystal, single-phase γ -InSe with a small amount of defects. We expect that the comprehensive demonstration of extensive γ -InSe deposition parameters presented in this work will help advance the field by providing a guidance system for the In-Se thin film phase and morphology landscape to accelerate 2D materials' application development and innovation.

AUTHOR INFORMATION

Corresponding Authors

Derrick S. H. Liu – Department of Materials Science and Engineering, The Pennsylvania State University, University Park, Pennsylvania 16802, United States; ⊚ orcid.org/0009-0002-9472-9347; Email: dxl457@psu.edu

Maria Hilse – Department of Materials Science and Engineering and 2D Crystal Consortium Material Innovation Platform, Materials Research Institute, The Pennsylvania State University, University Park, Pennsylvania 16802, United States; Email: mxh752@psu.edu

Authors

Andrew R. Lupini — Center for Nanophase Materials Sciences, Oak Ridge National Laboratory, Oak Ridge, Tennessee 37923, United States

Joan M. Redwing — Department of Materials Science and Engineering and 2D Crystal Consortium Material Innovation Platform, Materials Research Institute, The Pennsylvania State University, University Park, Pennsylvania 16802, United States; orcid.org/0000-0002-7906-452X

Roman Engel-Herbert – Paul-Drude-Institut für Festkörperelektronik, Leibniz-Institut im Forschungsverbund Berlin e.V., Berlin 10117, Germany

Complete contact information is available at: https://pubs.acs.org/10.1021/acsanm.3c02602

Author Contributions

D.S.H.L. conducted the thin film synthesis, material characterization, data analysis, and manuscript writing. M.H. provided help in paper editing and review, and data analysis. A.R.L. performed the STEM imaging. J.M.R. participated in coordinating this work. R.E.-H. designed the experiment and supervised this project. All authors contributed to the review of the manuscript.

Funding

U.S. Department of Energy, Office of Science, Office of Basic Energy Sciences Energy Frontier Research Center programs under Award no. DE-SC0021118. NSF cooperative Agreements Number DMR-1539916 and DMR-2039351. U.S. Department of Energy, Office of Basic Energy Sciences, Division of Materials Sciences and Engineering, and Center for Nanophase Materials Sciences, a U.S. Department of Energy, Office of Science User Facility at Oak Ridge National Laboratory under Contract no. DE-AC05-00OR22725.

Notes

The authors declare no competing financial interest.

ACKNOWLEDGMENTS

The experimental work, sample characterizations, and data analysis were supported by the Center for 3D Ferroelectric Microelectronics, an Energy Frontier Research Center funded by the U.S. Department of Energy, Office of Science, Office of Basic Energy Sciences Energy Frontier Research Center programs under Award Number DE-SC0021118. The research used equipment in the 2D Crystal Consortium-Materials Innovation Platform (2DCC-MIP) facility at Penn State, which is supported by the National Science Foundation under cooperative agreements DMR-1539916 and DMR-2039351. Electron microscopy and analysis were supported by the U.S. Department of Energy, Office of Basic Energy Sciences, Division of Materials Sciences and Engineering and by the Center for Nanophase Materials Sciences, a U.S. Department of Energy Office of Science User Facility at Oak Ridge National Laboratory.

REFERENCES

- (1) Sucharitakul, S.; Goble, N. J.; Kumar, U. R.; Sankar, R.; Bogorad, Z. A.; Chou, F. C.; Chen, Y. T.; Gao, X. P. A. Intrinsic Electron Mobility Exceeding 10³ cm²/(V·s) in Multilayer InSe FETs. *Nano Lett.* **2015**, *15* (6), 3815–3819.
- (2) Bandurin, D. A.; Tyurnina, A. V.; Yu, G. L.; Mishchenko, A.; Zólyomi, V.; Morozov, S. V.; Kumar, R. K.; Gorbachev, R. V.; Kudrynskyi, Z. R.; Pezzini, S.; Kovalyuk, Z. D.; Zeitler, U.; Novoselov, K. S.; Patanè, A.; Eaves, L.; Grigorieva, I. V.; Fal'Ko, V. I.; Geim, A. K.; Cao, Y. High Electron Mobility, Quantum Hall Effect and Anomalous Optical Response in Atomically Thin InSe. *Nat. Nanotechnol.* 2017, 12 (3), 223–227.
- (3) Yang, Z.; Jie, W.; Mak, C. H.; Lin, S.; Lin, H.; Yang, X.; Yan, F.; Lau, S. P.; Hao, J. Wafer-Scale Synthesis of High-Quality Semiconducting Two-Dimensional Layered InSe with Broadband Photoresponse. *ACS Nano* **2017**, *11* (4), 4225–4236.
- (4) Singh, P.; Baek, S.; Yoo, H. H.; Niu, J.; Park, J. H.; Lee, S. Two-Dimensional CIPS-InSe van Der Waal Heterostructure Ferroelectric Field Effect Transistor for Nonvolatile Memory Applications. *ACS Nano* **2022**, *16* (4), 5418–5426.
- (5) Chang, H. C.; Tu, C. L.; Lin, K. I.; Pu, J.; Takenobu, T.; Hsiao, C. N.; Chen, C. H. Synthesis of Large-Area InSe Monolayers by Chemical Vapor Deposition. *Small* **2018**, *14* (39), No. 1802351.
- (6) Chang, K.; Liu, J.; Lin, H.; Wang, N.; Zhao, K.; Zhang, A.; Jin, F.; Zhong, Y.; Hu, X.; Duan, W.; Zhang, Q.; Fu, L.; Xue, Q.-K.; Chen, X.; Ji, S.-H. Discovery of Robust In-Plane Ferroelectricity in Atomic-Thick SnTe. *Science* **2016**, *353* (6296), 274–278.
- (7) Wan, S.; Li, Y.; Li, W.; Mao, X.; Zhu, W.; Zeng, H. Room-Temperature Ferroelectricity and a Switchable Diode Effect in Two-Dimensional α -In₂Se₃ Thin Layers. *Nanoscale* **2018**, *10* (31), 14885–14892.
- (8) Cui, C.; Hu, W. J.; Yan, X.; Addiego, C.; Gao, W.; Wang, Y.; Wang, Z.; Li, L.; Cheng, Y.; Li, P.; Zhang, X.; Alshareef, H. N.; Wu, T.; Zhu, W.; Pan, X.; Li, L. J. Intercorrelated In-Plane and Out-of-Plane Ferroelectricity in Ultrathin Two-Dimensional Layered Semiconductor In₂Se₃. *Nano Lett.* **2018**, *18* (2), 1253–1258.
- (9) Guan, Z.; Hu, H.; Shen, X.; Xiang, P.; Zhong, N.; Chu, J.; Duan, C. Recent Progress in Two-Dimensional Ferroelectric Materials. *Adv. Electron. Mater.* **2020**, *6* (1), No. 1900818.
- (10) Chen, Y. L.; Analytis, J. G.; Chu, J.-H.; Liu, Z. K.; Mo, S.-K.; Qi, X. L.; Zhang, H. J.; Lu, D. H.; Dai, X.; Fang, Z.; Zhang, S. C.; Fisher, I. R.; Hussain, Z.; Shen, Z.-X. Experimental Realization of a Three-Dimensional Topological Insulator, Bi₂Te₃. *Science* **2009**, 325 (5937), 178–181.
- (11) Zhang, Y.; He, K.; Chang, C. Z.; Song, C. L.; Wang, L. L.; Chen, X.; Jia, J. F.; Fang, Z.; Dai, X.; Shan, W. Y.; Shen, S. Q.; Niu, Q.; Qi, X. L.; Zhang, S. C.; Ma, X. C.; Xue, Q. K. Crossover of the Three-Dimensional Topological Insulator Bi₂Se₃ to the Two-Dimensional Limit. *Nat. Phys.* **2010**, *6* (8), 584–588.
- (12) Wang, G.; Zhu, X.; Wen, J.; Chen, X.; He, K.; Wang, L.; Ma, X.; Liu, Y.; Dai, X.; Fang, Z.; Jia, J.; Xue, Q. Atomically Smooth Ultrathin Films of Topological Insulator Sb₂Te₃. *Nano Res.* **2010**, 3 (12), 874–880
- (13) Zhang, W.; Yu, R.; Zhang, H. J.; Dai, X.; Fang, Z. First-Principles Studies of the Three-Dimensional Strong Topological Insulators Bi_2Te_3 , Bi_2Se_3 and Sb_2Te_3 . New J. Phys. **2010**, 12, No. 065013.
- (14) Hasan, M. Z.; Kane, C. L. Colloquium: Topological Insulators. *Rev. Mod. Phys.* **2010**, 82 (4), 3045–3067.
- (15) Liu, D.; Zhang, W.; Mou, D.; He, J.; Ou, Y. B.; Wang, Q. Y.; Li, Z.; Wang, L.; Zhao, L.; He, S.; Peng, Y.; Liu, X.; Chen, C.; Yu, L.; Liu, G.; Dong, X.; Zhang, J.; Chen, C.; Xu, Z.; Hu, J.; Chen, X.; Ma, X.; Xue, Q.; Zhou, X. J. Electronic Origin of High-Temperature Superconductivity in Single-Layer FeSe Superconductor. *Nat. Commun.* **2012**, *3*, 931.
- (16) Lu, J. M.; Zheliuk, O.; Leermakers, I.; Yuan, N. F. Q.; Zeitler, U.; Law, K. T.; Ye, J. T. Evidence for Two-Dimensional Ising Superconductivity in Gated MoS₂. *Science* **2015**, 350 (6266), 1353–1357.

- (17) Wang, H.; Huang, X.; Lin, J.; Cui, J.; Chen, Y.; Zhu, C.; Liu, F.; Zeng, Q.; Zhou, J.; Yu, P.; Wang, X.; He, H.; Tsang, S. H.; Gao, W.; Suenaga, K.; Ma, F.; Yang, C.; Lu, L.; Yu, T.; Teo, E. H. T.; Liu, G.; Liu, Z. High-Quality Monolayer Superconductor NbSe₂ Grown by Chemical Vapour Deposition. *Nat. Commun.* **2017**, 8 (1), 394.
- (18) Saito, Y.; Nojima, T.; Iwasa, Y. Highly Crystalline 2D Superconductors. *Nat. Rev. Mater.* **2017**, 2 (1), 16094.
- (19) Mudd, G. W.; Svatek, S. A.; Ren, T.; Patanè, A.; Makarovsky, O.; Eaves, L.; Beton, P. H.; Kovalyuk, Z. D.; Lashkarev, G. V.; Kudrynskyi, Z. R.; Dmitriev, A. I. Tuning the Bandgap of Exfoliated InSe Nanosheets by Quantum Confinement. *Adv. Mater.* **2013**, 25 (40), 5714–5718.
- (20) Brotons-Gisbert, M.; Andres-Penares, D.; Suh, J.; Hidalgo, F.; Abargues, R.; Rodríguez-Cantó, P. J.; Segura, A.; Cros, A.; Tobias, G.; Canadell, E.; Ordejón, P.; Wu, J.; Martínez-Pastor, J. P.; Sánchez-Royo, J. F. Nanotexturing to Enhance Photoluminescent Response of Atomically Thin Indium Selenide with Highly Tunable Band Gap. *Nano Lett.* **2016**, *16* (5), 3221–3229.
- (21) Kuroda, N.; Nishina, Y. Resonance Raman Scattering Study on Exciton and Polaron Anisotropies in InSe. *Solid State Commun.* **1980**, 34 (6), 481–484.
- (22) Tamalampudi, S. R.; Lu, Y. Y.; Kumar, U. R.; Sankar, R.; Liao, C. D.; Moorthy, B. K.; Cheng, C. H.; Chou, F. C.; Chen, Y. T. High Performance and Bendable Few-Layered InSe Photodetectors with Broad Spectral Response. *Nano Lett.* **2014**, *14* (5), 2800–2806.
- (23) Lei, S.; Ge, L.; Najmaei, S.; George, A.; Kappera, R.; Lou, J.; Chhowalla, M.; Yamaguchi, H.; Gupta, G.; Vajtai, R.; Mohite, A. D.; Ajayan, P. M. Evolution of the Electronic Band Structure and Efficient Photo-Detection in Atomic Layers of InSe. *ACS Nano* **2014**, 8 (2), 1263–1272.
- (24) Luo, W.; Cao, Y.; Hu, P.; Cai, K.; Feng, Q.; Yan, F.; Yan, T.; Zhang, X.; Wang, K. Gate Tuning of High-Performance InSe-Based Photodetectors Using Graphene Electrodes. *Adv. Opt. Mater.* **2015**, 3 (10), 1418–1423.
- (25) Bergeron, H.; Guiney, L. M.; Beck, M. E.; Zhang, C.; Sangwan, V. K.; Torres-Castanedo, C. G.; Gish, J. T.; Rao, R.; Austin, D. R.; Guo, S.; Lam, D.; Su, K.; Brown, P. T.; Glavin, N. R.; Maruyama, B.; Bedzyk, M. J.; Dravid, V. P.; Hersam, M. C. Large-Area Optoelectronic-Grade InSe Thin Films via Controlled Phase Evolution. *Appl. Phys. Rev.* **2020**, *7* (4), No. 041402.
- (26) Balakrishnan, N.; Steer, E. D.; Smith, E. F.; Kudrynskyi, Z. R.; Eaves, Z. D. K.; Patanè, L. A.; Beton, P. H. Epitaxial Growth of γ -InSe and α , β , and γ -In₂Se₃ on ε -GaSe. 2D Mater. **2018**, 5 (111), No. 035026.
- (27) Zhou, J.; Shi, J.; Zeng, Q.; Chen, Y.; Niu, L.; Liu, F.; Yu, T.; Suenaga, K.; Liu, X.; Lin, J.; Liu, Z. InSe Monolayer: Synthesis, Structure and Ultra-High Second-Harmonic Generation. 2D Mater. 2018, 5 (2), No. 025019.
- (28) Huang, W.; Huang, W.; Gan, L.; Li, H. Phase-Engineered Growth of Ultrathin InSe Flakes by Chemical Vapor Deposition for High-Efficiency Second Harmonic Generation. *Chem. Eur. J.* **2018**, 24 (58), 15678–15684.
- (29) Kibirev, I. A.; Matetskiy, A. V.; Zotov, A. V.; Saranin, A. A. Thickness-Dependent Transition of the Valence Band Shape from Parabolic to Mexican-Hat-like in the MBE Grown InSe Ultrathin Films. *Appl. Phys. Lett.* **2018**, *112* (19), 191602.
- (30) Matetskiy, A. V.; Kibirev, I. A.; Mihalyuk, A. N.; Eremeev, S. V.; Zotov, A. V.; Saranin, A. A. Synthesis and Electronic Properties of InSe Bi-Layer on Si(111). *Appl. Surf. Sci.* **2020**, 539, No. 148144.
- (31) Zhang, Z.; Yuan, Y.; Zhou, W.; Chen, C.; Yuan, S.; Zeng, H.; Fu, Y. S.; Zhang, W. Strain-Induced Bandgap Enhancement of InSe Ultrathin Films with Self-Formed Two-Dimensional Electron Gas. *ACS Nano* **2021**, *15* (6), 10700–10709.
- (32) Wu, C. H.; Huang, Y. C.; Ho, Y. T.; Chang, S. J.; Wu, S. K.; Huang, C. H.; Chou, W. C.; Yang, C. S. Solid Phase Epitaxy of Single Phase Two-Dimensional Layered InSe Grown by MBE. *Nanomaterials* **2022**, *12* (14), 2435.

- (33) Honig, R. RB-104 RCA Labs 1957 Vapor Pressure Data for the More Common Elements. *RCA Review*, 1957; pp 195–204. https://tinyurl.com/2ezx8ne6.
- (34) Okamoto, H. In-Se (Indium-Selenium). J. Phase Equilibria Diffus. 2004, 25 (2), 201.
- (35) Kennedy, K.; Stefansky, T.; Davy, G.; Zackay, V. F.; Parker, E. R. Rapid Method for Determining Ternary-Alloy Phase Diagrams. *J. Appl. Phys.* **1965**, *36* (12), 3808–3810.
- (36) Zhang, H. T.; Zhang, L.; Mukherjee, D.; Zheng, Y. X.; Haislmaier, R. C.; Alem, N.; Engel-Herbert, R. Wafer-Scale Growth of VO_2 Thin Films Using a Combinatorial Approach. *Nat. Commun.* **2015**, *6*, 8475.
- (37) Liu, Y.; Weinert, M.; Li, L. Spiral Growth without Dislocations: Molecular Beam Epitaxy of the Topological Insulator Bi₂Se₃ on Epitaxial Graphene/SiC(0001). *Phys. Rev. Lett.* **2012**, *108* (11), No. 115501.
- (38) Nie, Y.; Barton, A. T.; Addou, R.; Zheng, Y.; Walsh, L. A.; Eichfeld, S. M.; Yue, R.; Cormier, C. R.; Zhang, C.; Wang, Q.; Liang, C.; Robinson, J. A.; Kim, M.; Vandenberghe, W.; Colombo, L.; Cha, P. R.; Wallace, R. M.; Hinkle, C. L.; Cho, K. Dislocation Driven Spiral and Non-Spiral Growth in Layered Chalcogenides. *Nanoscale* **2018**, *10* (31), 15023–15034.
- (39) Zhao, Y.; Kong, X.; Shearer, M. J.; Ding, F.; Jin, S. Chemical Etching of Screw Dislocated Transition Metal Dichalcogenides. *Nano Lett.* **2021**, *21* (18), 7815–7822.
- (40) Yang, S. K.; Peter, S.; Takoudis, C. G. Fundamentals of Two-Step Etching Techniques for Ideal Silicon-Hydrogen Termination of Silicon(111). *J. Appl. Phys.* **1994**, *76* (7), 4107–4112.
- (41) Vinh, L. T.; Eddrief, M.; Sbbenne, C. A.; Jussieu, P.; Gunther, R. Low Temperature Formation of Si (111) 7×7 Surfaces from Chemically Prepared H/Si (111) (1 × 1) Surfaces. *Appl. Phys. Lett.* **1994**, *64* (111), 3308–3310.
- (42) Dumas, P.; Chabal, Y. J.; Gunther, R.; Ibrahimi, A. T.; Petroff, Y. Vibrational Characterization and Electronic Properties of Long Range-Ordered, Ideally Hydrogen-Terminated Si(111). *Prog. Surf. Sci.* 1995, 48 (1–4), 313–324.
- (43) Scherrer, P. Bestimmung Der Grösse Und Der Inneren Struktur von Kolloidteilchen Mittels Röntgenstrahlen. Nachrichten von der Gesellschaft der Wissenschaften zu Göttingen, Math. Klasse 1918, 98–100.
- (44) Langford, J. I.; Wilson, A. J. C. Scherrer after Sixty Years: A Survey and Some New Results in the Determination of Crystallite Size. *J. Appl. Crystallogr.* **1978**, *11* (2), 102–113.
- (45) Ino, S. An Investigation of the Si(111) 7×7 Surface Structure by RHEED. *Jpn. J. Appl. Phys.* **1980**, *19* (7), 1277–1290.
- (46) Wu, Z.-C. Reflection High-Energy Electron Diffraction Pattern Calculations for Si(111)- 7 × 7 Surface. *J. Vac. Sci. Technol., B* **1988**, 6 (4), 1457.
- (47) Qian, G. X.; Chadi, D. J. Si(111)- 7 × 7 Surface: Energy-Minimization Calculation for the Dimer Adatom Stacking-Fault Model. *Phys. Rev. B* **1987**, 35 (3), 1288–1293.
- (48) Štich, I.; Payne, M. C.; King-Smith, R. D.; Lin, J.-S.; Clarke, L. J. Ab Initio Total-Energy Calculations for Extremely Large Systems: Application to the Takayanagi Reconstruction of Si(111). *Phys. Rev. Lett.* **1992**, *68* (9), 1351–1354.
- (49) Takahashi, K.; Nara, C.; Yamagishi, T.; Onzawa, T. Calculation of Surface Energy and Simulation of Reconstruction for Si(111) 3×3 , 5×5 , 7×7 , and 9×9 DAS Structure. *Appl. Surf. Sci.* **1999**, *151* (3), 299–301.
- (50) Herman, M. A.; Sitter, H. High-Vacuum Growth and Processing Systems. *BT Molecular Beam Epitaxy: Fundamentals and Current Status*; Herman, M. A.; Sitter, H., Eds.; Springer Berlin Heidelberg: Berlin, Heidelberg, 1996; pp 81–134.
- (51) Liu, D. S. H.; Hilse, M.; Engel-Herbert, R. Sticking Coefficients of Selenium and Tellurium. *J. Vac. Sci. Technol., A* **2021**, 39 (2), No. 023413
- (52) Liu, D. S. H.; Hilse, M.; Engel-Herbert, R. Desorption Characteristics of Selenium and Tellurium Thin Films. *J. Vac. Sci. Technol., A* **2022**, 40 (5), No. 053407.

DOI: 10.26207/qakv-p610.

(53) Köhler, U.; Demuth, J. E.; Hamers, R. J. Scanning Tunneling Microscopy Study of Low-temperature Epitaxial Growth of Silicon on Si(111)-(7 × 7). *J. Vac. Sci. Technol., A* 1989, 7 (4), 2860–2867. (54) Becker, R. S.; Golovchenko, J. A.; McRae, E. G.; Swartzentruber, B. S. Tunneling Images of Atomic Steps on the Si(111) 7 × 7 Surface. *Phys. Rev. Lett.* 1985, 55 (19), 2028–2031. (55) Liu, D. S. H.; Hilse, M.; Lupini, A. R.; Redwing, J. M.; Engel-Herbert, R. InSe on 3 in. Si(111) wafer-scale synthesis with combinatorial growth approach by MBE. ScholarSphere. 2023,